Evaluation of tropical water vapour from CMIP6 GCMs using the ESA CCI "Water Vapour" climate data records

Jia He[1], Helene Brogniez[1], and Laurence Picon[2]

[1]LATMOS/IPSL, UVSQ Université Paris-Saclay, CNRS, Guyancourt, France
[2]LMD/IPSL, Sorbonne-Université, CNRS, Paris, France

Correspondence: Jia He (jia.he@latmos.ipsl.fr) Helene Brogniez (helene.brogniez@latmos.ipsl.fr)

Abstract. The tropospheric water vapour data record generated within the ESA Climate Change Initiative "Water Vapour" project (ESA TCWV-COMBI) is used to evaluate the interannual variability of global climate models (CMIP6 framework under AMIP scenarios) and reanalysis (ECMWF ERA5). The study focuses on the tropical belt, with a separation of oceanic and continental situations. The intercomparison is performed according to the probability density function (PDF) of the total column water vapour (TCWV) defined yearly from the daily scale, as well as its evolution with respect to large-scale overturning circulation. The observational diagnostic relies on the decomposition of the tropical atmosphere into percentile of the PDF and into dynamical regimes defined from the atmospheric vertical velocity. Large variations are observed in the patterns among the data records, especially over tropical-land, while oceanic situations show more similarities in both interannual variations and percentile extremes. The signatures of El Nino/La Nina events, driven by the sea surface temperatures, are obvious over the oceans. Differences also occur over land for both trends (a strong moistening is observed in the ESA TCWV-COMBI data record which is absent in CMIP6 models and ERA5) and extremes years. The discrepancies are probably associated with the scene selection applied in the data process. Since the results are sensitive to the scene selection applied in the data process, discrepancies are observed among the datasets. Therefore, the normalization process is employed to analyse the time evolution with respect to the mean state. Other sources of differences, linked to the models and their parametrizations, are highlighted.

1 Introduction

Water vapour is short-lived yet sufficiently abundant component of the atmosphere that has both direct and indirect impact on weather and environment. It is one of the most important greenhouse gases and it plays a critical role in the hydrological cycle and climate system (Held and Soden, 2000). It is a radiatively important atmospheric constituent that influences atmospheric energy exchange through interactions with solar and thermal radiations (Raval and Ramanathan, 1989) with strong positive feedbacks (Sherwood et al., 2010). The precipitable water, mainly concentrated in the atmospheric boundary layer, is directly influenced by the surface temperature through robust thermodynamical constraints. The concentration of boundary layer water vapour will increase up to 7% /°C globally, confirmed by simulations and observations (Allan et al., 2014). Overall an increase in atmospheric moisture drives amplifying feedbacks, yielding to changes in evaporation and precipitation patterns at a global scale and to amplify heavy precipitation events (Hartmann et al., 2013; Allan et al., 2020).

25 Whether it is for weather forecasting, for understanding the evolution of cloud cells or for climate change studies, observing the distribution of atmospheric water vapour at any point in the atmosphere is a central issue. That is why the Global Climate Observing System (GCOS) declared the atmospheric water vapour as one of the Essential Climate Variables (ECVs) (GCOS, 2016). However, there are almost 5 orders of magnitude on the water vapour concentration between the surface and the top of the meteorological atmosphere. Evapotranspiration over continental surfaces, atmospheric dynamics or cloud formation

30 reinforce the horizontal and vertical gradients. Unfortunately, the required accuracy at all spatial and temporal scales is difficult to achieve, which leads to the combination of different types of measurements, each with their strengths and weaknesses, depending on the objectives (Wulfmeyer et al., 2015).

Satellite observations provide global water vapour measurements since the 1970s. Current sensors allow to observe the spatial distribution of water vapour according to three quantities: the vertical profile of specific humidity (q, in kg/kg), the relative

35 humidity of the upper troposphere (UTH, in %) and the total water vapour content (TCWV, in kg/m2). These sensors are deployed either in polar orbit, geostationary orbit or inclined orbit to enhance the temporal sampling of a latitude band. Many programs have been developed to get long-term observations with high spatial and temporal resolutions. Among them, the European Space Agency (ESA) Climate Change Initiative (CCI) program has been created to explore the full potential of its Earth Observation missions and to generate climate data record (CDR) associated to each of the 23 ECVs. Among the ESA

40 CCI projects, the CCI Water Vapour project (hereafter CCI_WV, https://climate.esa.int/en/projects/water-vapour) started in 2018 with the objectives to generate long-term coherent datasets of tropospheric and stratospheric water vapour.

The tropical belt (30°S-30°N) is a pivotal region in the Earth's climate. In this part of the globe, regional variations of the hydrological cycle are closely related to the Hadley-Walker overturning cells, that define the tropospheric circulation, and to its long-term changes (such as its observed slowdown and poleward expansion (Ma et al., 2018; Lu et al., 2007)).

45 Studies linking tropical climate evolution and water vapour distribution are done with both models and long-term observations. For instance, the infrared (IR) observations from the High resolution Infrared Radiation Sounder (HIRS) instrument have been used to investigate the interannual variability of tropical moisture of an atmospheric model (Huang et al., 2005). Following the same approach Chung et al. (2011) have analyzed the variability of the simulated UTH from a climate model using both IR and microwave measurements and showed that the wet bias of the model was related to errors in simulating the intensity of large-

50 scale circulation. Globally, improvements have been noticed in the simulation of the tropospheric water vapour distribution and variability between the Coupled Model Intercomparison Project (CMIP5, release in 2014) and the earlier CMIP3 excercise (release in 2010) (Jiang et al., 2012). However while the models perform best for the boundary layers over the oceans, most likely thanks to the thermodynamic constraint imposed by the sea surface temperature, strong biases remain in the upper layers of the troposphere, where clouds and atmospheric dynamics have large uncertainties.

55 A recent intercomparison work of a selection of available long-term datasets has been conducted under the auspices of the Global Energy and Water Exchanges (GEWEX) program of the world climate research programme (WCRP) (Schröder et al., 2019). This intercomparison not only highlighted the complementarity among the sensors, but also underlined the caveats in the studies of trends and variabilities induced by artificial break points contained in the CDRs such as calibration changes, retrieval algorithms, resolution changes that impact the sampling, etc.. Apart from these important points that are inherent to

the development of robust time series suitable to investigate climate variability, the evaluation of the distribution and variability of the water vapour with respect to large-scale circulation is still of upmost importance. The last IPCC assessment report (AR6, 2021) contains an entire chapter on water cycle that highlights the role of the large-scale atmospheric circulation in driving regional changes of atmospheric moisture fluxes and in position and strength of the tropical rain belt (Arias et al., 2021). The present work follows the previous analysis framework proposed by Bony et al. (2004) and investigates the the variabiltity of total column water vapour (TCWV) of a selection of Global Climate Models (GCMs) that have participated in the CMIP6 exercise (Eyring et al., 2016). The ESA CCI_WV CDRs are studied from the aspect of the large-scale circulation. Section 2 describes the various datasets: the ESA CCI_WV CDRs, the CMIP6 GCMs and the ERA5 reanalysis. Section 3 is dedicated to the method of evaluation itself, while Section 4 discusses the results. Finally the conclusions are drawn in Section 5.

2 Data Description

We focus on the tropical belt (30°S - 30°N). Data obtained from ESA CCI_WV, CMIP6 GCMs, and ERA5 reanalysis are studied at daily scale and over the period 2003 - 2014. The monthly atmospheric vertical velocity at 500hPa ($\omega 500$) of each data record is used as a proxy of large-scale circulation following Bony et al. (2004). Note that the vertical velocity from ERA5 is also used as the dynamical reference for the CCI_WV CDRs.

2.1 ESA CCI_WV Climate Data Records

The Phase 1 of the ESA CCI_WV project was dedicated to built climate records of both tropospheric and stratospheric water vapour. The project provides daily and monthly water vapour observations on the global scale with spatial resolution of 0.5 and 0.05 degree for the period of 2002-2017.

The TCWV is commonly defined as the vertically integrated water vapour over the full column with units of kg/m^2. Observations from microwave (MW) imagers (namely SSM/I, SSMIS, AMSR-E and TMI) over the ice-free ocean, partly based on a fundamental CDR (Fennig et al., 2020), and near-infrared (NIR) imagers (including MERIS, MODIS-Terra and OLCI) over land, coastal ocean and sea-ice have been combined within the ESA CCI_WV project. Details of the retrieval is discussed in Andersson et al. (2010) and Schröder et al. (2013) for the MW imagers. The algorithm for NIR imagers are discussed in Lindstrot et al. (2012), Diedrich et al. (2015) and Preusker et al. (2021). The MW and NIR data streams are processed independently and combined afterwards so that the individual TCWV values and their uncertainties remain unchanged. Validation of the dataset against GRUAN and SuomiNet show that the bias and corrected RMSD (cRMSD) are generally small and within ±1.5 kg/m^2 and 2.5 kg/m^2, respectively. The available spatial resolutions of the combined data record (hereafter TCWV-COMBI) are 0.5°x0.5° and 0.05°x0.05°, where the NIR based data are averaged and the MW-based data are oversampled to produce the results with desired resolution. The daily and monthly mean data are available for TCWV-COMBI product during July 2002 - December 2017. Table 1 summarizes the various original data sources that are used in the TCWV-COMBI CDR.

Here we use the daily / 0.05°x0.05° TCWV-COMBI dataset. However, as detailed above the data processing of the TCWV-

Table 1. Summary of the characteristics of CCI water vapour data TCWV-COMBI.

Data source	Spectral domains	Region	Data description	Spatial resolution	Time span	Reference
MERIS	NIR	Land, coastal and sea-ice	Daytime, cloud free	1200 m	2002 - 2012	Fischer and Bennartz (1997)
MODIS	NIR	Land, coastal and sea-ice	Daytime, cloud free	1000 m	2011 - 2017	Gao and Kaufman (2003)
OLCI	NIR	Land, coastal and sea-ice	Daytime, cloud free	1200 m	2016 - 2017	Lindstrot et al. (2012)
HOAPS	MW	Ocean	6-hourly composites, without strong precipitation	0.5°degrees	2002 - 2017	Lindstrot et al. (2014)

COMBI is different between land and ocean which then impact the processing of the CMIP6 models: over land areas TCWV is estimated under cloud-free conditions, while over ocean areas TCWV is estimated until heavy precipitation occurs. Moreover the evaluation period is restricted to before 2014 for consistency with the available period of the CMIP6 experiment. Such cut in the ESA TCWV-COMBI excludes the OLCI observations.

2.2 CMIP6 Models

Seven GCMs participating to CMIP6 are evaluated here, limited by the availability of the required geophysical variables at daily resolution (at least) that is comparable with the CCI_WV CDRs. However, there was no TCWV field at the daily frequency that was available from the Earth System Grid Federation (ESGF) (node of Institut Pierre Simon Laplace, IPSL). Therefore we recomputed TCWV from the vertical profiles of specific humidity q (in g/kg) that were provided at the model vertical resolution. High vertical resolution of specific humidity (more than 19 vertical levels in the troposphere) were then necessary to be certain to capture the full tropospheric water vapour (using the extraction on a selection of pressure levels would bias the computation of TCWV).

The TCWV (in kg/m^2) from each model is thus calculated using:

$$TCWV = \int_{surface}^{top} q \frac{\mathrm{d}p}{g} \tag{1}$$

where g is the gravitational acceleration constant, and dp is the difference between adjacent pressure levels (hPa).

We focus on the AMIP (Atmospheric Model Inter-comparison Project) (Ackerley et al., 2018) scenario with prescribed time-varying sea surface temperature (SST) and sea-ice concentrations from observations and includes variations in natural and anthropogenic external forcings (Eyring et al., 2016). The detailed model descriptions are listed in Table 2. In addition to the CMIP6 models, the ensemble mean of the seven models is also included in the following analysis to represent the mean state of the CMIP6 models.

Since the TCWV-COMBI data is cloud screened over land area, it is important to carefully analyze the cloud conditions for CMIP6 models before making the quantitative comparison. The cloud screening of the model-to-observation approach must remove the cloudy pixels while maintaining enough data for further evaluation. Since cloud fraction (cf) is the only parameter that is available for the CMIP6 models to be employed as the indicator for cloudiness, a series of threshold tests were conducted by screening the pixels with cf values larger than 5%, 25%, 50%, and 75% at all pressure levels. The distribution of TCWV

Table 2. Main characteristics of the seven CMIP6 models of the study along with TCWV-COMBI and ERA5. The percentages over land and ocean are computed once the scene selection is applied.

Institution	Model ID	Horizontal resolution	Vertical resolution	Percentage of land data (%)	Percentage of ocean data (%)	Reference
CCCma	CanESM5	2.81° × 2.81°	49 Levels (1- 1022 hPa)	55.63%	99.89%	Swart et al. (2019)
CNRM-CERFACS	CNRM-CM6-1	1.41°×1.41°	91 Levels ((0.1 - 1039 hPa))	62.85%	99.86%	Voldoire et al. (2019)
	CNRM-ESM2-1	1.41°×1.41°	91 Levels (0.1 - 1039 hPa)	62.81%	99.86%	Séférian et al. (2019)
IPSL	IPSL-CM6A-LR	1.25°×2.50°	79 Levels (0 - 1028 hPa)	76.10%	99.79%	Lurton et al. (2020)
MPI-M	MPI-ESM1-2-HR	0.94°×0.94°	95 Levels (0 - 1055 hPa)	69.90%	99.98%	Müller et al. (2018)
NCAR	CESM2	0.94°×1.25°	32 Levels (4 - 993 hPa)	47.14%	99.97%	Danabasoglu et al. (2020)
	CESM2-WACCM	0.94°×1.25°	70 Levels (0 - 993 hPa)	46.14%	99.97%	Gettelman et al. (2019)
ESA CCI_WV	TCWV-COMBI	0.05°×0.05°	-	43.73%	99.82%	Ref as in Table 1
ECMWF	ERA5	0.5°×0.5°	-	52.76%	97.14%	Hersbach et al. (2020)

over tropical land from CanESM5 of the CMIP6 model with different cloud masks, along with data from TCWV-COMBI and ERA5, are shown in Figure 1. The results indicate that data with cf less than 50% at all pressure levels show a reasonable spatial coverage comparable to TCWV-COMBI and ERA5. Therefore, this threshold is adopted as the general cloud mask for the CMIP6 models, although this cannot be considered a purely clear sky. It is worth mentioning that since the results are dependent on the cloud masks, the normalization process is also included in the following analysis to better illustrate the time evolution with respect to the mean state instead of strict biases.

The description of the datasets remaining for the following analysis after the cloud screening over the land and the ocean is displayed in Table 2. Over land, the percentage of data remained for the CMIP6 models after the cloud screening are globally in the range 46.14% - 76.10%. Over tropical oceans the percentage of data remained is higher and range from 99.79% to 99.98%. Although the scene selection is more stringent over land, this indicates that the CMIP6 data used in the following analysis are comparable in terms of size of sample to the data from TCWV-COMBI and ERA5. It is worth mentioning that although the screening thresholds for the models are set to meet the criteria of the TCWV-COMBI product, the number of data retained for the comparison are not exactly the same for all models. Therefore, differences among data sets may be observed in the analysis. This is particularly true over tropical land.
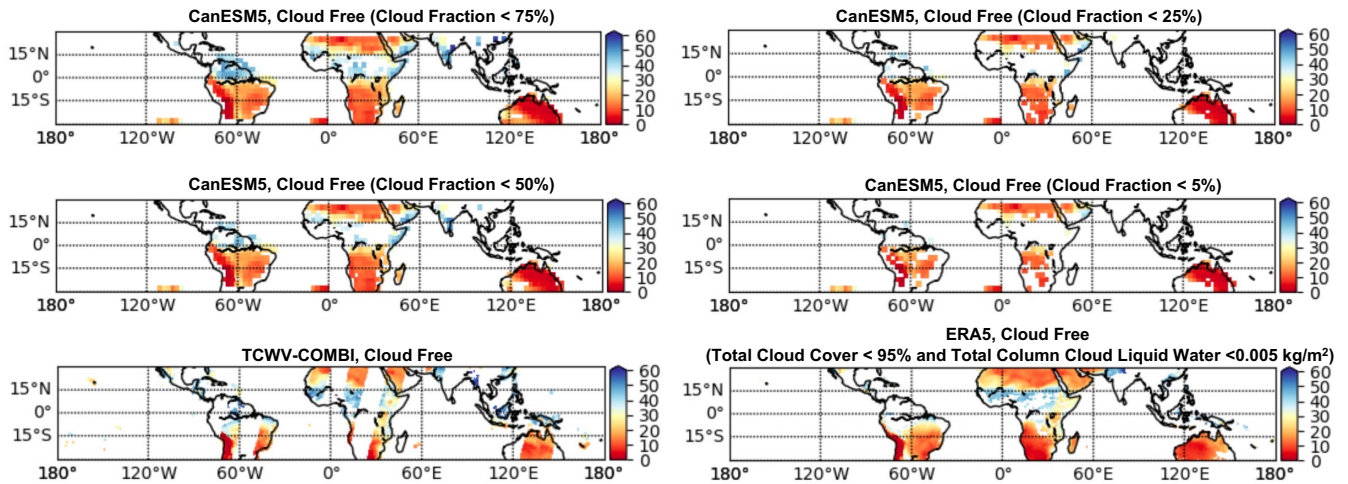
Figure 1. Examples of daily mean TCWV over tropical land obtained from CanESM5 with different cloud mask (pixels with cloud fraction larger than 75%, 50%, 25%, and 5% at all pressure levels are considered as clouded) along with data from TCWV-COMBI and ERA5, July 1st 2003.

2.3 ERA5

The reanalysis data are widely analyzed in atmospheric sciences to assess the impact of changes in observation system, to scale progress in model simulations, and to calculate climatology for forecast-error evaluation (Hersbach et al., 2020). The ECMWF's ERA5 TCWV data are based on the integrated forecasting system (IFS) Cy41r2, with considerably enhanced

135   horizontal resolution of 31 km compared to 80 km for ERA-Interim. Here the ERA5 TCWV with hourly frequency are averaged into daily data. To compare the data under the same conditions, the ERA5 land-sea mask is employed for land and ocean separation, and a scene selection is performed and is similar to the process of the CMIP6 data. Hence, data with total cloud cover less than 95% and total column cloud liquid water less than 0.005 kg/m^2 over land (Sohn and Bennartz, 2008), and data with total precipitation less than 0.001 kg/m^2/s^2 over ocean are retained.

140   **3   Methods**

The time series of the daily means of the CMIP6, ERA5 and ESA CCI_WV TCWV-COMBI are analyzed with tropical-land and tropical-ocean separation over the common observation period that covers July 2003 to December 2014.

The intercomparisons are conducted according to two approaches:

1) The first approach evaluates the interannual variation of TCWV based on the probability distribution function (PDF) estab-

145   lished from the daily records for each year of the period. The percentiles of the TCWV are defined from the yearly distributions and the data is sorted by intervals of 10 percentiles. Finally, the mean TCWV of each interval is computed and normalized by the corresponding mean TCWV of the whole observation period for this given percentile.This is generalized for every per-

centile. This approach is meant to highlight the tropical anomalies with respect to the mean and trace back to the inter-annual variability of the tropical atmosphere.

 2) The second approach is based on the fact that the water vapour distribution is strongly controlled by the large-scale vertical
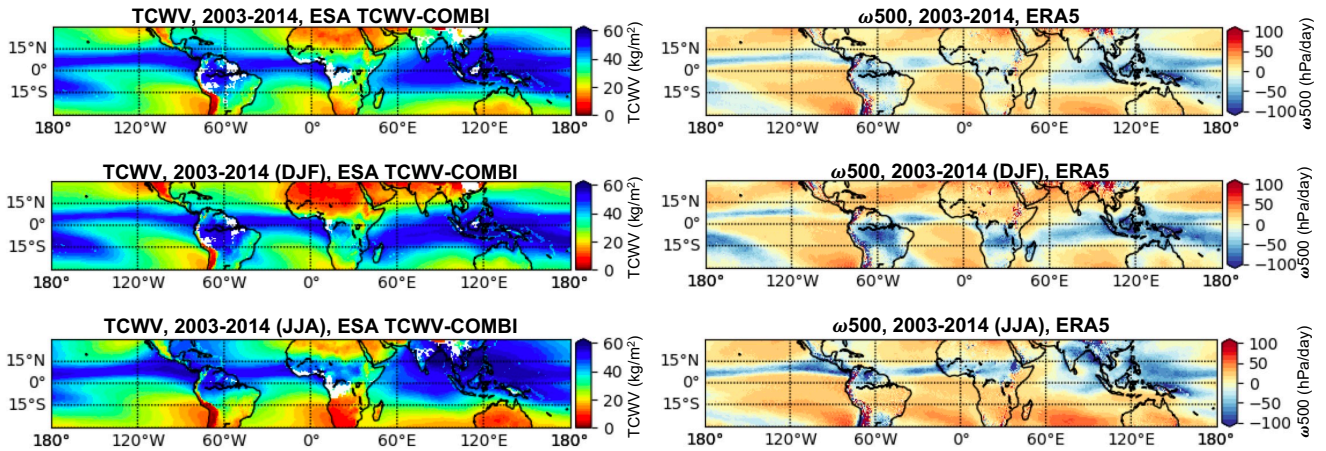
Figure 2. Maps of the TCWV-COMBI (in kg/m^2) during 2003 - 2014 for the tropical region (30°S - 30°N) for the whole period, Winter (December, January and February - DJF), and Summer (June, July, and August - JJA) and the corresponding maps of ERA5 $\omega500$ (in hPa/day).

150

motion of the atmosphere. Therefore, we can use the mid-tropospheric atmospheric vertical velocity at 500 hPa (noted $\omega500$ in hPa/day) as a proxy for the vertical motions in the tropics (Bony et al., 2004). While such framework has been greatly used to study tropical clouds and their distribution (e.g., Konsta et al., 2012; Höjgård-Olsen et al., 2020), this link between vertical motion and TCWV is documented (e.g., Brogniez and Pierrehumbert, 2007) and further illustrated on Figure 2. Figure

155 2 presents the TCWV-COMBI averaged over the whole 2003-2014 period as well as the mean Winter (December, January, and February - DJF) and mean Summer (June, July, and August - JJA), together with the corresponding $\omega500$ taken from ERA5 at a monthly scale. As expected, a moist troposphere is associated with large-scale ascending motion ($\omega500 < 0$ hPa/day) while a dry troposphere is associated with large-scale subsidence ($\omega500 > 0$ hPa/day). The TCWV data are sorted upon 10hPa/day-bins of monthly values of $\omega500$. The dynamical decomposition is performed for all TCWV data records at each year of the

160 time period. Moreover the TCWV data averaged over the whole 2003-2014 period is also sorted into the corresponding $\omega500$ bins of the period and this value is considered as the reference to normalize the results. This second approach allows to study the trends in TCWV for a given state of the large-scale dynamics, and thus overcome issues associated with variations (such as shifts or expansion) of the atmospheric circulation (Vallis et al., 2015; Mbengue and Schneider, 2017).

4 Results and Discussions

This section aims to assess the degree of agreement in the TCWV climatology and interannual variations between the ESA CCI_WV TCWV-COMBI, CMIP6 models and ERA5 reanalysis data over the tropics (30°S - 30°N). The distribution of the water vapour over tropics and its link to large-scale circulation ($\omega500$) are discussed in detail.

4.1 Description of the tropical TCWV: 2003-2014

4.1.1 Time series

Figure 3 shows the time series of the TCWV of the different datasets over land (Fig. 3a; clear skies only) and over ocean (Fig. 3b; all-weather without heavy precipitation) for the period 07/2003-12/2014. There are differences in the range of daily mean TCWV exists some differences, but all datasets have the same changing tendency. Overall, the different data records agree well with each other despite some 'outliers' observed over tropical-land in TCWV-COMBI data that resulted from the differences in available sample size under the clear-sky condition each day. Strong seasonal variations are observed over tropical land with minima reached during JFM and maxima reached during JJA and with a very weak interannual variability. Since the results are dependent on the cloud-screen process, the detailed discussions on the impact of ENSO events are discussed in following section 4.2. Over the tropical oceans, the seasonal variations are softer (the minima still occur during JFM, but the maxima are not always reached in JJA) with a strong interannual signal.

More specifically, the ESA TCWV-COMBI data is moister than ERA5 and most CMIP6 models over both the land and the ocean areas, and this moist bias is even more pronounced over tropical land (Fig. 3a, 10kg/m^2 over land vs 2kg/m^2 over ocean). On the other hand, the daily mean values of water vapour concentration over ocean areas are higher than the values over land areas. This difference can be explained because the TCWV datasets over land areas are composed of clear-sky-only data, which are likely drier than the nearby cloud area for a given location and thus translates into a dry bias associated with moistening processes by convective clouds (Sohn et al., 2006). Hence, the cloud screening over land makes it difficult to compare the datasets directly. In addition, since the boundary layer is drier in the continental subtropics and the maritime stratocumulus zones are wetter at low levels, the ocean areas should appear moister than the land areas.

4.1.2 The distribution of tropical TCWV

The normalized PDFs of the daily TCWV obtained from all data records over both land and ocean are displayed in Figure 4. The bimodal distributions can be explained by the presence of more humid columns in the Intertropical Convergence Zone (ITCZ) and relatively drier ones in subtropical regions. Similar to the time series analysis, the characteristics over land are significantly different with the results over ocean area because of the data screening. Over land, all datasets reach a first maximum at around 10-13 kg/m^2 and present a secondary maximum near 40-50 kg/m^2. Moreover, more lower values are observed in the CMIP6 models and ERA5 than in the ESA TCWV-COMBI dataset and this cannot be explained by the cloud-screening method alone. Indeed, the results of simulation models and ERA5 are dependent on cloud conditions, consequently will lead to differences
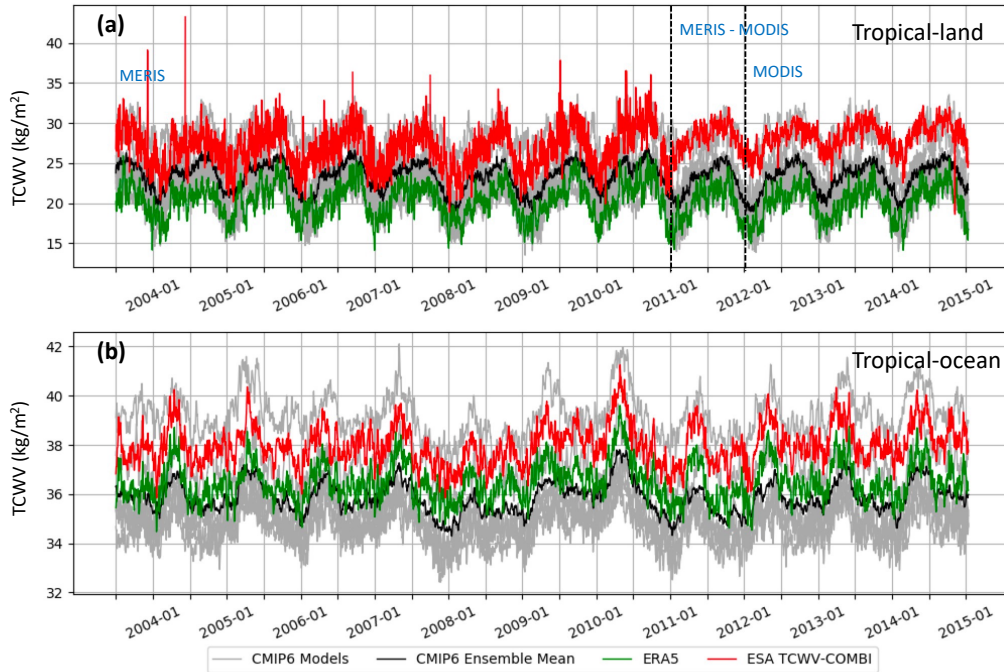
Figure 3. Time series of daily mean TCWV in the tropics (30°S - 30°N) over (a) land areas under clear-sky condition and (b) ocean areas except for heavy precipitation (see details in Section 2). The time series cover the period 07/2003-12/2014. The gray lines denote the individual CMIP6 models while the black line represents their ensemble mean. The green line represents ERA5 and the red line is the ESA CCI_WV TCWV-COMBI.

195   in the comparison. For instance, the ESA TCWV-COMBI dataset is strictly cloud-free while some cloudy scenes remain in both ERA5 and CMIP6 (see Section 2), which could translate in a moister TCWV of the latter data records. Although there are changes in variability in TCWV-COMBI data over tropical land with the inclusion of MODIS since 2011, validation of the dataset against GRUAN and SuomiNet shows that the dataset is stable and accurate during the whole observation period. Over oceans, most of the TCWV data are located around 20-60 kg/m^2. The main peak is around 30 kg/m^2, and a secondary

200   peak appears near 50 kg/m^2. While the mean peak of PDF is nearly identical for TCWV-COMBI, ERA5 and CMIP6, there is a divergence for the secondary peak. This secondary peak even dominates the PDF of the CMIP6 models while ERA5 and ESA TCWV-COMBI are still quite similar.

4.1.3   Extremes of the distributions

The data records are then evaluated following the approach (1) described in Section 3: the percentiles of the annual distributions

205   of TCWV (at daily resolutions) are sorted into bins of 10% intervals, and this is done for each year of the period.

The normalized TCWV for land areas and sorted by 10%-percentiles intervals for each year are displayed in Figure 5. The bluish colors indicate that the TCWV value of the interval is larger than the reference value, indicating wet anomalies. The
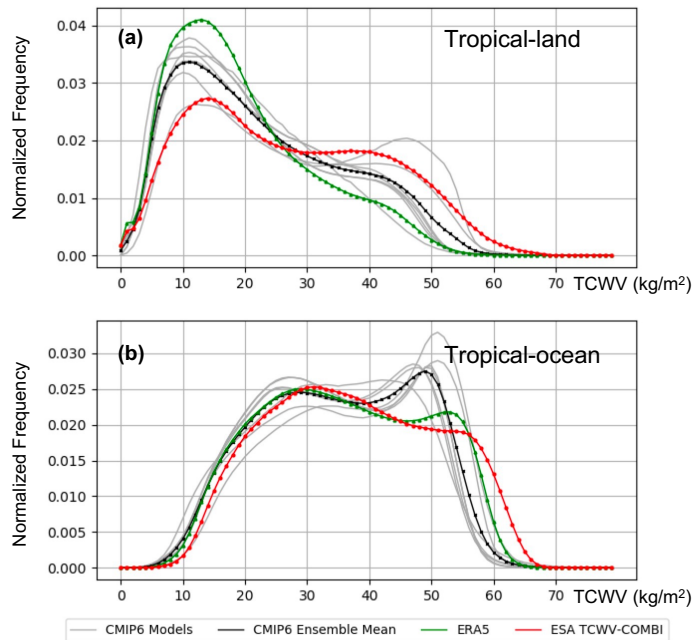
Figure 4. The normalized PDFs of the TCWV in the tropical area (30°S-30°N) over (a) land areas (under clear-sky only condition), and over (b) ocean areas (under all-weather condition except for heavy precipitation). The gray lines denote the individual CMIP6 models while the black line represents their ensemble mean. The green line represents ERA5 and the red line is the ESA CCI+ TCWV-COMBI.

reddish colors indicate that the TCWV value is smaller than the reference, indicating dry anomalies. As shown in the figure, the ESA TCWV-COMBI data have quite different characteristics compared to CMIP6 and ERA5 results. A clear moistening trend is observed in the drier percentiles of TCWV-COMBI record. The tiping point seems to be 2011 and thus may be caused by the inhomogeneity of cloud-mask products for different observation instruments when computing the ESA TCWV-COMBI data. Indeed, the data record merged NIR observation from MERIS over 2002-2012 and MODIS observation are included over 2011-2017. Despite individual discrepancies, the CMIP6 ensemble mean is in good agreement with the ERA5 data. Overall, anomalies are observed in the time period for all data records: 2008 appears as a dry year while 2010 reveals a clear signal of humidification, especially over the high parts of the distributions of TCWV (percentiles > 60%) of TCWV.

A similar comparison is performed over the tropical oceans and the results are shown in Figure 6. The TCWV-COMBI results are well coincident with CMIP6 models and ERA5 data. Dry anomalies are observed in 2004 for the ESA TCWV-COMBI and ERA5 in the dry end of TCWV. Dry anomalies are also observed in 2008 and 2011 over the highest percentiles (> 60%) for all data records, while 2008 is the driest year of the period. Wet anomalies are observed in 2010 for the highest percentiles in all data records. ERA5 also reveals 2012 as a moister year, in the low range of TCWV, but this anomalous year is not present in the ESA TCWV-COMBI or CMIP6 ensemble mean. The very good agreement among the various data sets is largely due to the fact that the CMIP6 models are evaluated under the AMIP scenario, so with the same prescribed SST for all models
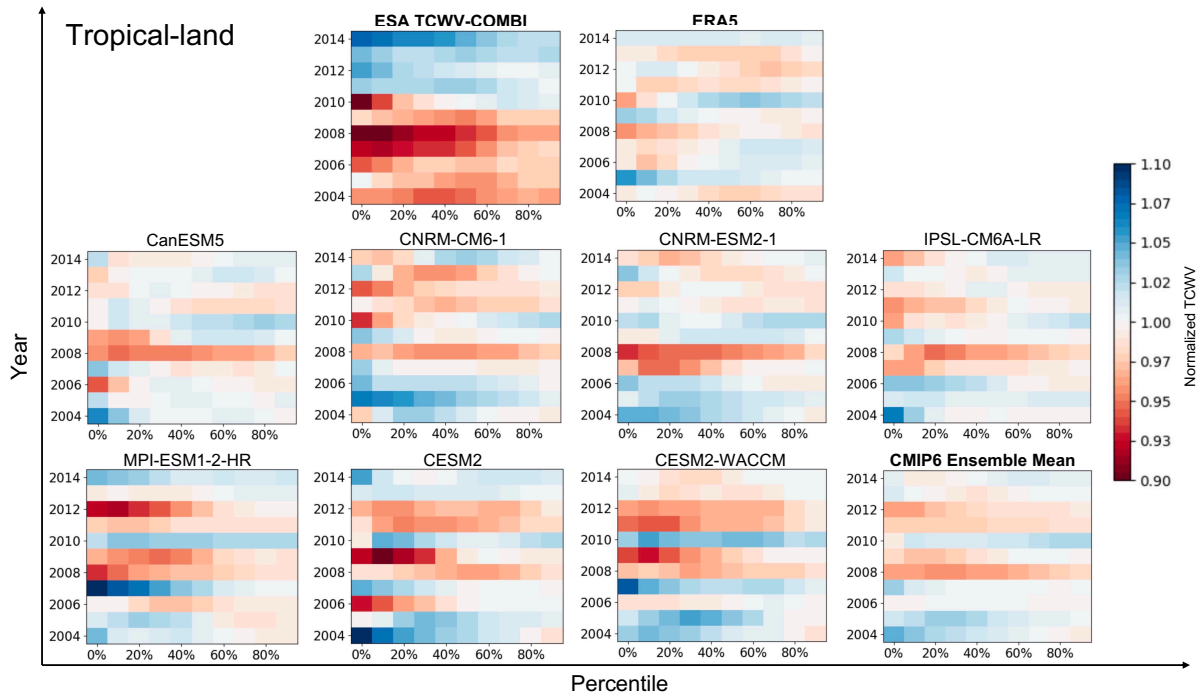
Figure 5. Normalized percentiles of the TCWV over land areas for every data record. The percentiles are grouped into bins of 10% intervals. The x-axis represents the percentiles intervals, and the y-axis represents the year. Note that the period starts in 2004 instead of 2003 to focus on full years.

and ERA5, and that the relationship between SST and TCWV is largely explained by the Clausius-Clapeyron law (Stephens, 1990). Hence this explains that anomalous years are the results of El Nino Southern Oscillation (Trenberth et al., 2005): 2008 and 2011 are characterized by a very negative ENSO index, while 2010 is an intermediate year, which starts with a positive ENSO cycle and is followed by a negative one.

4.2 TCWV and large-scale circulation

4.2.1 General assessment

The interannual variability of TCWV is then analyzed from its links with the large-scale atmospheric circulation, and follows the approach (2) described in Section 3. The monthly $\omega500$ of individual data records are decomposed into 10 hPa/day intervals in the range of -120 to 120 hPa/day. Figure 7 displays the normalized PDFs of the $\omega500$ of the CMIP6 models and ERA5. As mentioned earlier there is no atmospheric circulation data from the ESA TCWV-COMBI data record, so the $\omega500$ from ERA5 is also employed as the reference for this dataset. Figure 7 (a) and (b) show that the PDFs of the $\omega500$ from the CMIP6 ensemble mean agrees well with the ERA5 data. Most of the $\omega500$ reside in around 10 - 20 hPa/day over both tropical-land and
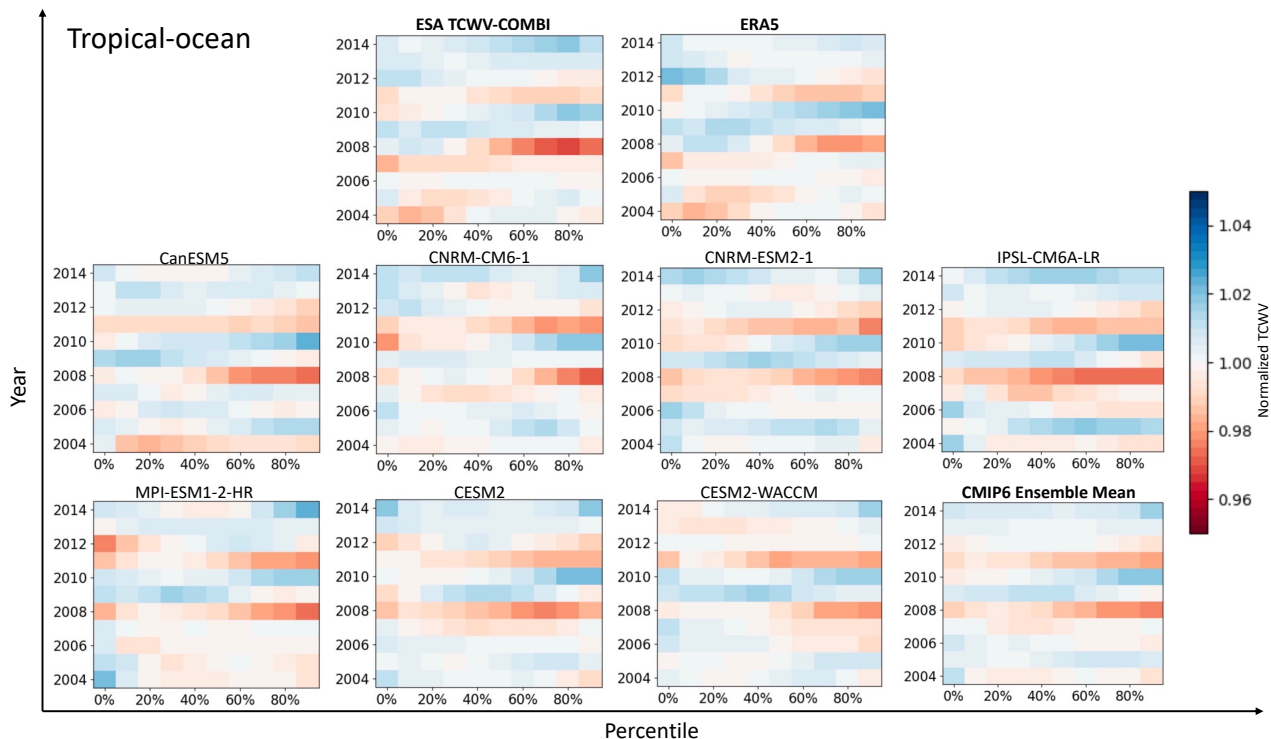
Figure 6. Same as Figure 5 but for oceans.

tropical-ocean area, which characterizes the dominance of the large-scale Hadley subsidence in subtropical free troposphere and explains the clear-sky radiative cooling of the tropics as discussed in Bony et al. (2004).

The TCWV of each dataset is then sorted into the vertical velocity bins by the corresponding value of $\omega 500$. Therefore, the variations of the TCWV can be analyzed from the perspective of atmospheric vertical motion. As shown in Figure 7 (c) and (d), large-scale downward motion is associated with a dry troposphere, while large-scale ascent is associated with a moister troposphere (except for ERA5 over land, where the most humid regimes are over weak subsidence). The results are in agreement with the maps of Figure 2. Overall, the CMIP6 models and ERA5 show differences with the ESA TCWV-COMBI data in the amplitude of the signal and in the gradient of moisture between the ascending and descending regions. The evaporation from the oceans is the primary source of water vapour in the atmosphere, the oceanic boundary layer is humid even in a weak subsidence regime. Besides, as the reference $\omega 500$ for TCWV-COMBI are from ERA5, it is sensible that there are differences observed in the TCWV-COMBI data as it stays humid in both upward and weak subsidence regions. While the large-scale atmospheric dynamics are consistent among the datasets, the discrepancies in the TCWV reveal difficulties in representing the moistening processes of the tropical atmosphere: lateral mixing (Pierrehumbert and Roca, 1998; Pierrehumbert, 1998), outflows from clouds, too high/too low precipitation efficiencies of the convective schemes (Brogniez and Pierrehumbert, 2007). It is worth mentioning that the moistest regime of TCWV from ERA5 over land areas occurred in a weak subsidence regime instead of
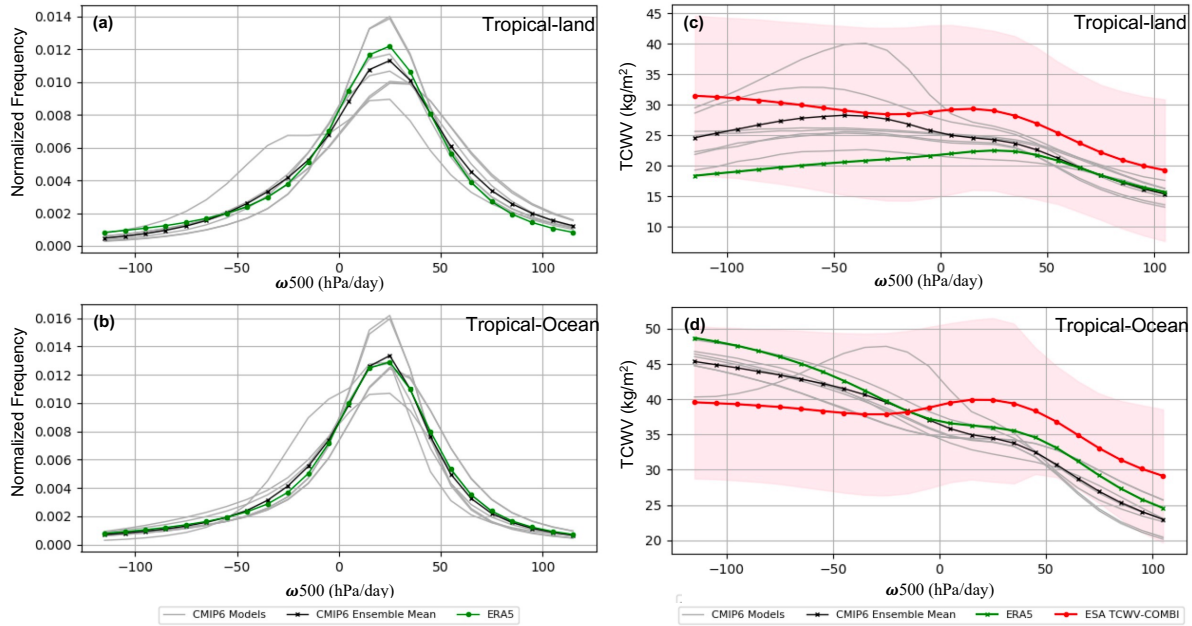
Figure 7. (Left) Normalized PDFs of $\omega500$ (in hPa/day) over land (a) and ocean (b) for CMIP6 models (grey lines), their ensemble mean (black line), as well as ERA5 (green line); (Right) Mean TCWV from the CMIP6 models (grey lines), their ensemble mean (black line), ERA5 (green line), and ESA TCWV-COMBI (red line) in different circulation regimes of $\omega500$ over land (c) and ocean (d) areas. The shaded area in pink represents the σ of each bin in TCWV-COMBI data.

the strong ascending region. This difference is partly because of the cloud screening processes. Therefore, the results could not accurately represent the large-scale advection humidification/drying processes.

4.2.2 Trends over lands

This global assessment is further discussed by applying the TCWV-$\omega500$ approach for every year of each data record to delineate the trends in TCWV. As shown in Figure 8, all the data records (except for ERA5) agree that the driest troposphere (red) are associated with the most positive $\omega500$ bins (meaning the areas of highest downward motion). The moistest troposphere, however, are not always located in the most negative $\omega500$ bins (the highest upward motion).

ERA5 and the CMIP6 ensemble mean display the lowest TCWV values (< 16kg/m^2) that occur all along the 2004-2014 period while the ESA TCWV-COMBI data record reaches values $\sim$18kg/m^2 and this minimum is reached over 2007-2008. There is also a very strong variability amongst the CMIP6 models: IPSL-CM6A-LR is clearly the moistest model and CanESM5 is the driest. The moist bias of IPSL-CM6A-LR is already documented (Boucher et al., 2020) and is explained by the (too) efficient parametrization scheme of the transport of evaporated air from the surface to the top of the boundary layer.The discrepancy observed from CanESM5 is partly because of its strong effective climate efficiency compared to all current CMIP6 models, as the positive low and non-low shortwave cloud feedbacks – particularly with regards to low clouds across the equatorial Pacific,
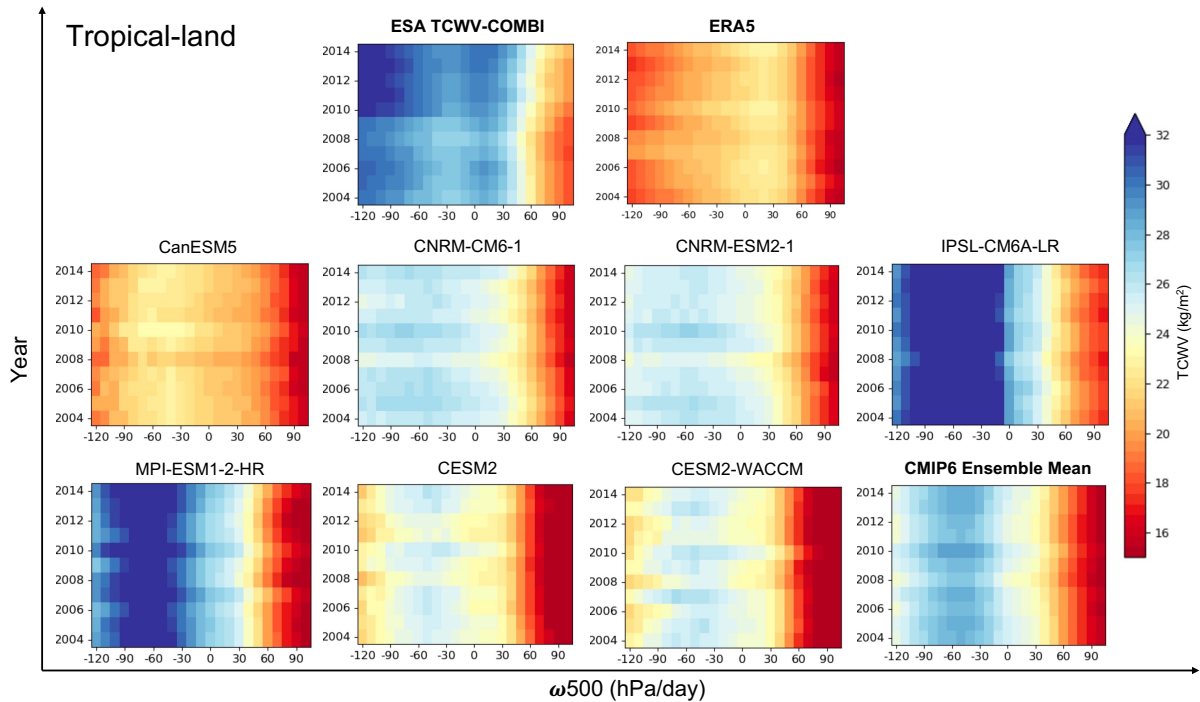
Figure 8. Mean of TCWV over tropical land areas at each dynamical intervals ($\omega500$) in 10 hPa/day computed from each data record.

as well as subtropical and extratropical free troposphere cloud optical depth – are the dominant contributors to CanESM5's

265   increased climate sensitivity (Virgin et al., 2021). ERA5 also displays a very dry troposphere at all dynamical regimes.

To unravel the anomalies of TCWV, the mean values of TCWV of each circulation regime observed during the whole comparison period (2004 - 2014) are employed as the reference to normalize the results. The normalized TCWV at each circulation interval for the different data records are displayed in Figure 9. Although different patterns are observed, dry anomalies occurred in 2008 in all of the data records (except for ERA5 (Du et al., 2021), where dry anomalies were observed for subsidence

270   and weak upward motion regimes), and wet anomalies occurred in 2010. These extreme years are consistent with the previous findings (section 4.1.3) and this second approach provides another angle of analysis on the assessment:

- The ESA TCWV-COMBI reveals a clear moistening tendency, especially over the subsiding branch of the atmospheric circulation after 2011. One of the major causes of the turning point is the inclusion of MODIS data since 2011 which would increase the sampling size of the data and in turn affect the tendency.

275
- The TCWV from ERA5 shows only extreme years but no distinct tendency. In the regions of highest upward motions, 2007 and 2008 appear moister than the other years while 2004 and 2013 appear drier. Once again, this may be due to the scene selection applied over land, but this would not explain entirely the differences with the ESA TCWV-COMBI.
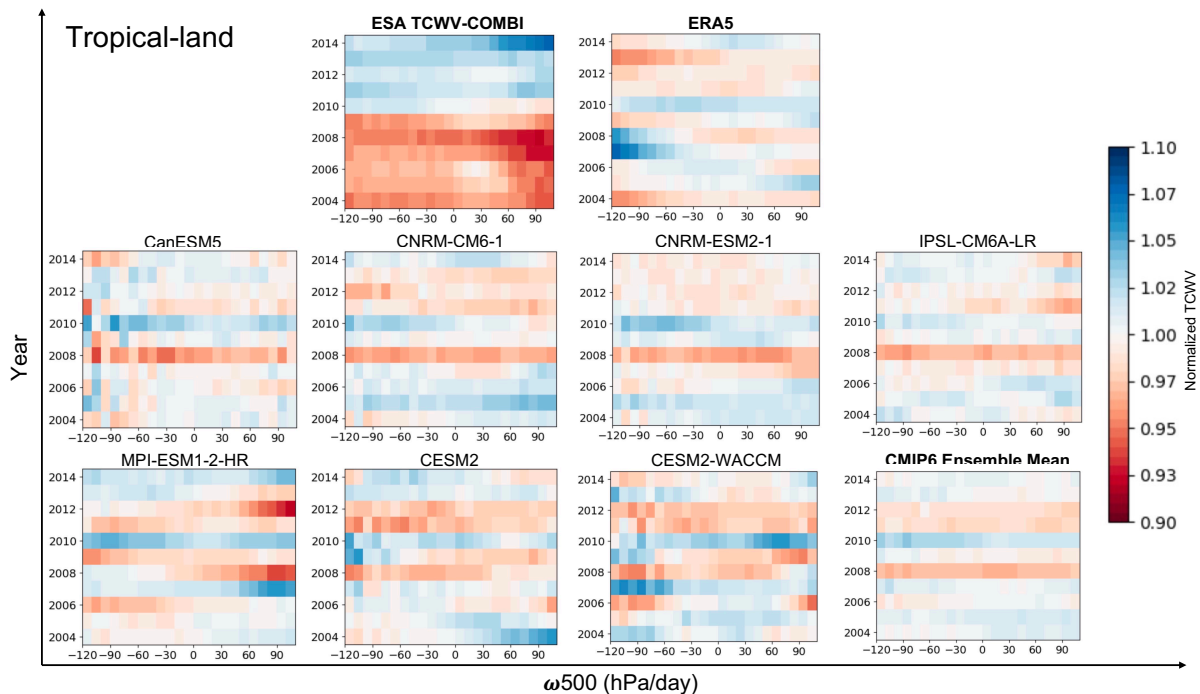
Figure 9. Normalized TCWV with respect to the 2004-2014 mean over tropical land areas at each dynamical intervals (ω500) in 10 hPa/day computed from each data record.

– Finally, the CMIP6 models and their ensemble mean show consistent interannual variabilities: dry anomalies occurred in 2008 in all the data records, and wet anomalies occurred in 2010. The results of the models are in a relative agreement

280   with ERA5 and ESA TCWV-COMBI.

4.2.3 Trends over oceans

Oceanic situations were also discussed with respect to the large-scale circulation. The results are shown in Figure 10 (mean TCWV) and Figure 11 (normalized TCWV). As the data over ocean areas are obtained under all-weather conditions except for heavy precipitation, the impacts from clear-sky biases are greatly reduced. All data records, except for TCWV-COMBI,

285   CanESM5 and IPSL-CM6A-LR, show that the strongest ascending zones are corresponding to the very humid regions. Different from the results over land, where the CMIP6 models showed strong differences (CanESM5 was driest and IPSL-CM6A-LR was the moistest), the amplitudes and gradients of moisture are closer to each other over oceans.Since the transport model in the boundary layer of IPSL-CM6A-LR affects both shallow and deep convection regimes, a compensational bias would be induced, thus a moist bias will be present in the weak upward motion regimes ($\sim$ -30 hPa/day) (Boucher et al., 2020). The

290   normalized TCWV with respect to dynamical intervals over ocean areas are shown in Figure 11. The temporal evolutions of TCWV-ω500 are consistent with the earlier analysis based on the temporal evolution of the percentiles of TCWV over ocean
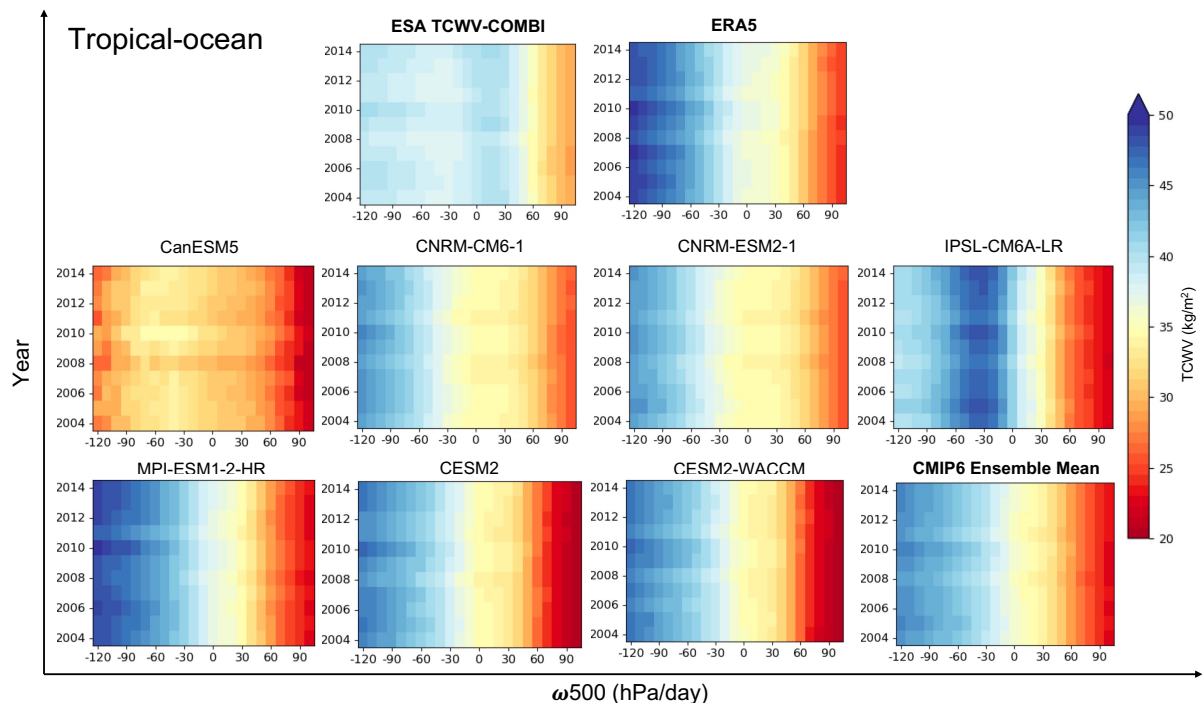
Figure 10. Mean of TCWV over tropical ocean areas at each dynamical intervals ($\omega 500$) in 10 hPa/day computed from each data record.

(section 4.1.3). The extreme dry and moist years (respectively 2008 and 2010) are the same between ESA TCWV-COMBI, ERA5 and the CMIP6 ensemble mean.

5 Conclusions

295 Despite the importance of water vapour in the study of climate variability, our ability to evaluate the water vapour feedback is constrained by its measurements at ranges of scales that are adapted for local, regional and global studies. This deficiency is attributable in part to the fact that it is difficult to quantitatively and accurately measure the distribution of water vapour. To work towards the requirement of GCOS on satellite-based water vapour observation as ECV, the ESA Climate Change Initiative "Water Vapour" project (ESA CCI_WV) tackled this challenge by generating gridded products on stratospheric and

300 tropospheric water vapour from multiple satellite observations suitable to climate and process studies.

We have conducted a comprehensive evaluation of the tropical water vapour (30°N-30°S) of seven GCMs (CMIP6 models, AMIP scenario) and ERA5 using the TCWV-COMBI climate data record developed within the ESA CCI_WV project as a reference. The study focused over tropical-land and tropical-ocean areas at the daily frequency and over the 2003-2014 period. The variability of TCWV was analyzed according to (i) its probability density function (PDF) defined at a yearly scale over

305 the period and (ii) to the large-scale circulation using the atmospheric vertical velocity at 500hPa ($\omega 500$) as a proxy of the
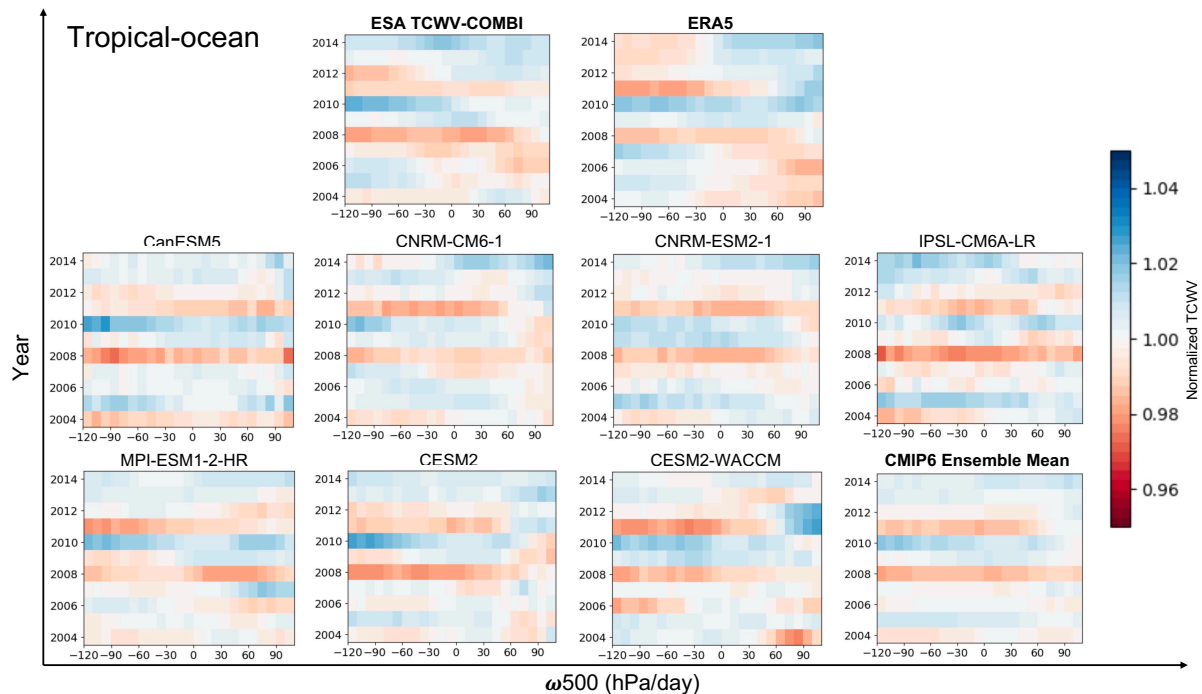
Figure 11. Normalized TCWV with respect to the 2004-2014 mean over tropical ocean areas at each dynamical intervals (ω500) in 10 hPa/day computed from each data record.

tropospheric overturning circulation.

Different patterns of variability are observed among the various datasets, the largest discrepancies being noticed over land areas, while over the oceans the datasets are closer to each other:

– over land, the PDFs of the ESA TCWV-COMBI present a clear moistening trend of their driest percentiles, with a tipping point in 2011, probably associated with the addition of the MODIS observation in the climate data record. The projection of the TCWV onto regimes of ω500 shows the same behavior, dry anomalies occurred in 2008 in all of the data records (except for ERA5, where dry anomalies were observed for subsidence and weak upward motion regimes), and wet anomalies occurred in 2010. Interestingly, the CMIP6 ensemble mean and the ERA5 reanalysis are in good agreement in terms of interannual anomalies, although the ERA5 TCWV is clearly too dry.

– over ocean, the PDFs of all datasets present the same interannual variability. The extreme dry and moist years, associated with El Nino and La Nina events, are the same. This similarities hold when using the large-scale circulation as an evaluation tool, with the same transition between the dry/subsiding regimes and the moister/ascending regimes.

The results show that the ESA TCWV-COMBI data and ERA5 data vary within the ensemble spread of CMIP6 models, indicating that the mean models could correctly represent the evolution of water vapour with respect to large-scale circulation.

320 The humid area is related with the ascending motion (negative value in $\omega 500$) and dry area is related with the subsiding motion (positive value in $\omega 500$) over both tropical land and tropical ocean area. There are discrepancies observed among the data records, probably caused by the lateral mixing, outflows from clouds, and the precipitation efficiencies of the convective schemes. It is difficult to track entirely the reasons of the differences, however, the differences and similarities can be explained by several factors:

325 1) the use of different satellites with different accuracies and resolutions within the ESA TCWV-COMBI may explain part of the moistening trend observed for this dataset over land.

2) the cloud-masks applied to the GCMs and ERA5 and defined to mimic the cloud-mask of the observation can also explain the differences.

3) the parametrization of the moisture fluxes at the surface and of convection, as well as the climate efficiency of the GCMs

330 also contribute to the observed differences.

4) the CMIP6 models under AMIP scenario (with prescribed sea surface temperatures), and the scene selection that is much more conservative than over land, explained the agreement between the ESA TCWV-COMBI, ERA5 and the GCMs over oceans.

It is really necessary to underline the role of the cloud mask in the assessment of water vapour fields in climate models

335 using observations, even though it's easier to compare water vapour than clouds. The water vapour profiles (and sometimes the integrated values) from climate models usually have coarser spatial resolution than satellite observations.The satellite measurements, on the other hand, are often strictly restrained by cloud contamination. This clearly shows the importance of having access to the simulated water vapour (full profiles as well as integrated values) for the clear sky part of the meshes of the climate models.

340 *Author contributions.* JH carried out the data analysis and prepared all the figures. JH, HB and LP contributed to the interpretation of the results and wrote the paper.

Competing interests. The authors do not declare any competing interests

Acknowledgements. The study was funded by ESA via the Water_Vapour_CCI project of ESA's Climate Change Initiative (CCI). The combined microwave and near-infrared imager based product COMBI was initiated, funded and ESA Water_Vapour_CCI project, with

345 contributions from Brockmann Consult, Spectral Earth, Deutscher Wetterdienst and the EUMETSAT Satellite Climate Facility on Climate Monitoring (CM SAF). The combined MW and NIR product will be owned by EUMETSAT CM SAF and will be released by CM SAF in late 2021. This study benefited from the ESPRI (Ensemble de Services Pour la Recherche à l'IPSL) computing and data center (https: //mesocentre.ipsl.fr).

References

Ackerley, D., Chadwick, R., Dommenget, D., and Petrelli, P.: An ensemble of AMIP simulations with prescribed land surface temperatures, Geoscientific Model Development, 11, 3865–3881, 2018.

Allan, R. P., Chunlei, L., Matthias, Z., A., L. D., E., K., and A., B.-S.: Physically consistent responses of the global atmospheric hydrological cycle in models and observations, Surveys in Geophysics, 35, 533–552, doi:10.1007/s10 712–012–9213–z, 2014.

Allan, R. P., Barlow, M., Byrne, M. P., Cherchi, A., Douville, H., Fowler, H. J., Gan, T. Y., Pendergrass, A. G., Rosenfeld, D., Swann, A. L., et al.: Advances in understanding large-scale responses of the water cycle to climate change, Annals of the New York Academy of Sciences, 1472, 49–75, 2020.

Andersson, A., Fennig, K., Klepp, C., Bakan, S., Graßl, H., and Schulz, J.: The Hamburg ocean atmosphere parameters and fluxes from satellite data–HOAPS-3, Earth System Science Data, 2, 215–234, 2010.

Arias, P., Bellouin, N., Coppola, E., Jones, R., Krinner, G., Marotzke, J., Naik, V., Palmer, M., Plattner, G.-K., Rogelj, J., et al.: Climate Change 2021: The Physical Science Basis. Contribution of Working Group14 I to the Sixth Assessment Report of the Intergovernmental Panel on Climate Change; Technical Summary, 2021.

Bony, S., Dufresne, J.-L., Le Treut, H., Morcrette, J.-J., and Senior, C.: On dynamic and thermodynamic components of cloud changes, Climate Dynamics, 22, 71–86, 2004.

Boucher, O., Servonnat, J., Albright, A. L., Aumont, O., Balkanski, Y., Bastrikov, V., Bekki, S., Bonnet, R., Bony, S., Bopp, L., et al.: Presentation and evaluation of the IPSL-CM6A-LR climate model, Journal of Advances in Modeling Earth Systems, 12, e2019MS002 010, 2020.

Brogniez, H. and Pierrehumbert, R. T.: Intercomparison of tropical tropospheric humidity in GCMs with AMSU-B water vapor data, Geophysical research letters, 34, 2007.

Chung, E.-S., Soden, B. J., Sohn, B.-J., and Schmetz, J.: Model-simulated humidity bias in the upper troposphere and its relation to the large-scale circulation, Journal of Geophysical Research: Atmospheres, 116, 2011.

Danabasoglu, G., Lamarque, J.-F., Bacmeister, J., Bailey, D., DuVivier, A., Edwards, J., Emmons, L., Fasullo, J., Garcia, R., Gettelman, A., et al.: The community earth system model version 2 (CESM2), Journal of Advances in Modeling Earth Systems, 12, 2020.

Diedrich, H., Preusker, R., Lindstrot, R., and Fischer, J.: Retrieval of daytime total columnar water vapour from MODIS measurements over land surfaces, Atmospheric Measurement Techniques, 8, 823–836, 2015.

Du, M., Huang, K., Zhang, S., Huang, C., Gong, Y., and Yi, F.: Water vapor anomaly over the tropical western Pacific in El Niño winters from radiosonde and satellite observations and ERA5 reanalysis data, Atmospheric Chemistry and Physics, 21, 13 553–13 569, 2021.

Eyring, V., Bony, S., Meehl, G. A., Senior, C. A., Stevens, B., Stouffer, R. J., and Taylor, K. E.: Overview of the Coupled Model Intercomparison Project Phase 6 (CMIP6) experimental design and organization, Geoscientific Model Development, 9, 1937–1958, 2016.

Fennig, K., Schröder, M., Andersson, A., and Hollmann, R.: A fundamental climate data record of SMMR, SSM/I, and SSMIS brightness temperatures, Earth System Science Data, 12, 647–681, 2020.

Fischer, J. and Bennartz, R.: Retrieval of total water vapour content from MERIS measurements, Algorithm Theoretical Basis Document PO-TN-MEL-GS, 5, 1997.

Gao, B.-C. and Kaufman, Y. J.: Water vapor retrievals using Moderate Resolution Imaging Spectroradiometer (MODIS) near-infrared channels, Journal of Geophysical Research: Atmospheres, 108, 2003.

GCOS: The Global Observing System for Climate : Implementation Needs, Tech. rep., available online at : https://library.wmo.int/opac/doc_num.php?explnum_id=3417, 2016.

Gettelman, A., Mills, M., Kinnison, D., Garcia, R., Smith, A., Marsh, D., Tilmes, S., Vitt, F., Bardeen, C., McInerny, J., et al.: The whole atmosphere community climate model version 6 (WACCM6), Journal of Geophysical Research: Atmospheres, 124, 12 380–12 403, 2019.

Hartmann, D. L., Tank, A. M. K., Rusticucci, M., Alexander, L. V., Brönnimann, S., Charabi, Y. A. R., Dentener, F. J., Dlugokencky, E. J., Easterling, D. R., Kaplan, A., et al.: Observations: atmosphere and surface, in: Climate change 2013 the physical science basis: Working group I contribution to the fifth assessment report of the intergovernmental panel on climate change, pp. 159–254, Cambridge University Press, 2013.

Held, I. M. and Soden, B. J.: Water vapor feedback and global warming, Annual review of energy and the environment, 25, 441–475, 2000.

Hersbach, H., Bell, B., Berrisford, P., Hirahara, S., Horányi, A., Muñoz-Sabater, J., Nicolas, J., Peubey, C., Radu, R., Schepers, D., et al.: The ERA5 global reanalysis, Quarterly Journal of the Royal Meteorological Society, 146, 1999–2049, 2020.

Höjgård-Olsen, E., Brogniez, H., and Chepfer, H.: Observed Evolution of the Tropical Atmospheric Water Cycle with Sea Surface Temperature, Journal of Climate, 33, 3449–3470, 2020.

Huang, X., Soden, B. J., and Jackson, D. L.: Interannual co-variability of tropical temperature and humidity: A comparison of model, reanalysis data and satellite observation, Geophysical research letters, 32, 2005.

Jiang, J. H., Su, H., Zhai, C., Perun, V. S., Del Genio, A., Nazarenko, L. S., Donner, L. J., Horowitz, L., Seman, C., Cole, J., et al.: Evaluation of cloud and water vapor simulations in CMIP5 climate models using NASA "A-Train" satellite observations, Journal of Geophysical Research: Atmospheres, 117, 2012.

Konsta, D., Chepfer, H., and Dufresne, J.-L.: A process oriented characterization of tropical oceanic clouds for climate model evaluation, based on a statistical analysis of daytime A-train observations, Climate dynamics, 39, 2091–2108, 2012.

Lindstrot, R., Preusker, R., Diedrich, H., Doppler, L., Bennartz, R., and Fischer, J.: 1D-Var retrieval of daytime total columnar water vapour from MERIS measurements, Atmospheric Measurement Techniques, 5, 631–646, 2012.

Lindstrot, R., Stengel, M., Schröder, M., Fischer, J., Preusker, R., Schneider, N., Steenbergen, T., and Bojkov, B.: A global climatology of total columnar water vapour from SSM/I and MERIS, Earth System Science Data, 6, 221–233, 2014.

Lu, J., Vecchi, G. A., and Reichler, T.: Expansion of the Hadley cell under global warming, Geophysical Research Letters, 34, 2007.

Lurton, T., Balkanski, Y., Bastrikov, V., Bekki, S., Bopp, L., Braconnot, P., Brockmann, P., Cadule, P., Contoux, C., Cozic, A., et al.: Implementation of the CMIP6 Forcing Data in the IPSL-CM6A-LR Model, Journal of Advances in Modeling Earth Systems, 12, 2020.

Ma, J., Chadwick, R., Seo, K.-H., Dong, C., Huang, G., Foltz, G. R., and Jiang, J. H.: Responses of the tropical atmospheric circulation to climate change and connection to the hydrological cycle, Annual Review of Earth and Planetary Sciences, 46, 549–580, 2018.

Mbengue, C. and Schneider, T.: Storm-track shifts under climate change: Toward a mechanistic understanding using baroclinic mean available potential energy, Journal of the Atmospheric Sciences, 74, 93–110, 2017.

Müller, W. A., Jungclaus, J. H., Mauritsen, T., Baehr, J., Bittner, M., Budich, R., Bunzel, F., Esch, M., Ghosh, R., Haak, H., et al.: A Higher-resolution Version of the Max Planck Institute Earth System Model (MPI-ESM1. 2-HR), Journal of Advances in Modeling Earth Systems, 10, 1383–1413, 2018.

Pierrehumbert, R.: Lateral mixing as a source of subtropical water vapor, Geophysical research letters, 25, 151–154, 1998.

Pierrehumbert, R. T. and Roca, R.: Evidence for control of Atlantic subtropical humidity by large scale advection, Geophysical Research Letters, 25, 4537–4540, 1998.

Preusker, R., Carbajal Henken, C., and Fischer, J.: Retrieval of Daytime Total Column Water Vapour from OLCI Measurements over Land Surfaces, Remote Sensing, 13, 932, 2021.

Raval, A. and Ramanathan, V.: Observational determination of the greenhouse effect, Nature, 342, 758–761, 1989.

425 Schröder, M., Jonas, M., Lindau, R., Schulz, J., and Fennig, K.: The CM SAF SSM/I-based total column water vapour climate data record: Methods and evaluation against re-analyses and satellite, Atmospheric Measurement Techniques, 6, 765–775, 2013.

Schröder, M., Lockhoff, M., Shi, L., August, T., Bennartz, R., Brogniez, H., Calbet, X., Fell, F., Forsythe, J., Gambacorta, A., et al.: The GEWEX water vapor assessment: Overview and introduction to results and recommendations, Remote Sensing, 11, 251, 2019.

Séférian, R., Nabat, P., Michou, M., Saint-Martin, D., Voldoire, A., Colin, J., Decharme, B., Delire, C., Berthet, S., Chevallier, M., et al.:
430 Evaluation of CNRM Earth System Model, CNRM-ESM2-1: Role of Earth System Processes in Present-Day and Future Climate, Journal of Advances in Modeling Earth Systems, 11, 4182–4227, 2019.

Sherwood, S., Roca, R., Weckwerth, T., and Andronova, N.: Tropospheric water vapor, convection, and climate, Reviews of Geophysics, 48, 2010.

Sohn, B.-J. and Bennartz, R.: Contribution of water vapor to observational estimates of longwave cloud radiative forcing, Journal of Geo-
435 physical Research: Atmospheres, 113, 2008.

Sohn, B.-J., Schmetz, J., Stuhlmann, R., and Lee, J.-Y.: Dry bias in satellite-derived clear-sky water vapor and its contribution to longwave cloud radiative forcing, Journal of climate, 19, 5570–5580, 2006.

Stephens, G. L.: On the relationship between water vapor over the oceans and sea surface temperature, Journal of Climate, 3, 634–645, 1990.

Swart, N. C., Cole, J. N., Kharin, V. V., Lazare, M., Scinocca, J. F., Gillett, N. P., Anstey, J., Arora, V., Christian, J. R., Hanna, S., et al.: The
440 canadian earth system model version 5 (CanESM5. 0.3), Geoscientific Model Development, 12, 4823–4873, 2019.

Trenberth, K. E., Fasullo, J., and Smith, L.: Trends and variability in column-integrated atmospheric water vapor, Climate dynamics, 24, 741–758, 2005.

Vallis, G. K., Zurita-Gotor, P., Cairns, C., and Kidston, J.: Response of the large-scale structure of the atmosphere to global warming, Quarterly Journal of the Royal Meteorological Society, 141, 1479–1501, 2015.

445 Virgin, J. G., Fletcher, C. G., Cole, J. N., von Salzen, K., and Mitovski, T.: Cloud Feedbacks from CanESM2 to CanESM5. 0 and their influence on climate sensitivity, Geoscientific Model Development, 14, 5355–5372, 2021.

Voldoire, A., Saint-Martin, D., Sénési, S., Decharme, B., Alias, A., Chevallier, M., Colin, J., Guérémy, J.-F., Michou, M., Moine, M.-P., et al.: Evaluation of CMIP6 deck experiments with CNRM-CM6-1, Journal of Advances in Modeling Earth Systems, 11, 2177–2213, 2019.

Wulfmeyer, V., Hardesty, R. M., Turner, D. D., Behrendt, A., Cadeddu, M. P., Di Girolamo, P., Schlüssel, P., Van Baelen, J., and Zus, F.:
450 A review of the remote sensing of lower tropospheric thermodynamic profiles and its indispensable role for the understanding and the simulation of water and energy cycles, Reviews of Geophysics, 53, 819–895, 2015.